1994A&A...282..605J

Astron. Astrophys. 282, 605–620 (1994)

ASTRONOMY
AND
ASTROPHYSICS

Physical and chemical structure of the IC 63 nebula

I. Millimeter and far–infrared observations

David J. Jansen[1], **Ewine F. van Dishoeck**[1], **and John H. Black**[2]

[1] Leiden Observatory, P.O. Box 9513, NL-2300 RA Leiden, The Netherlands
[2] Steward Observatory, University of Arizona, Tucson, AZ 85721, USA

Received February 16, accepted August 7, 1993

Abstract. We present results of a (sub)millimeter and far–infrared study of the reflection/emission nebula IC 63, located close to the B0.5p star γ Cas. The source has been mapped in the ^{12}CO $2 \rightarrow 1$ and $3 \rightarrow 2$, ^{13}CO $2 \rightarrow 1$, and CS $2 \rightarrow 1$ lines and shows a small molecular cloud less than $1' \times 2'$ in extent, which coincides with the brightest optical nebulosity and IRAS 100 μm emission. IC 63 is therefore an excellent example of a nearby ($d \approx 230$ pc), edge–on photon–dominated region (PDR). Various other molecules have been observed at the peak position through their rotational transitions, in order to probe the physical parameters and to derive abundances. The measured CO, HCO^+, HCN, CS and H_2CO line ratios suggest that the cloud is warm, $T \approx 50$ K, and dense, $n(H_2) \approx 5 \times 10^4$ cm^{-3}. Excitation of molecules by electrons may play a significant role in this PDR. On the basis of these physical conditions, column densities have been determined from the observed line strengths. Several different methods are discussed to constrain the H_2 column density, including the use of measured submillimeter continuum fluxes. The resulting abundances of species such as CN and CS are similar to those found in cold, dark clouds like TMC–1 and L134N. However, the abundances of other simple molecules such as HNC, HCO^+, N_2H^+ and possibly C_2H are lower by factors of at least three, probably because of the enhanced photodissociation rates at a distance of 1.3 pc from a B star. Surprisingly, only the abundance of the H_2S molecule appears enhanced. More complex, volatile molecules such as CH_3OH, CH_3CN and HNCO, and the sulfur–oxides SO and SO_2 have not been found in this cloud. Limited observations of molecules in the reflection nebula NGC 2023 are presented as well, and the resulting molecular abundances are compared with those found for IC 63.

Key words: ISM: individual objects: IC 63 – ISM: individual objects: NGC 2023; reflection nebulae – radio lines: interstellar

1. Introduction

The conditions in molecular clouds can be perturbed either through heating by ultraviolet photons or by the passage of shock waves. The effect that these processes have on the chemical abundances is not well established observationally, but is of great importance for the interpretation of molecular line observations not only in our own Galaxy, but also in external galaxies. In order to gain a better understanding of the similarities and differences between the effects of these two heating mechanisms, we have started a detailed study of a few clouds which might serve as templates of either nearly–pure photon–dominated regions (PDRs) or nearly–pure shocks. In this paper we present results of a study of a nearly–pure PDR: the reflection/emission nebula IC 63.

IC 63 is a reflection nebula associated with the B0.5 IVpe star γ Cas (HD 5394), which lies at a distance of approximately 230 pc (Vakili et al. 1984). The projected distance between IC 63 and the star is 20′, corresponding to 1.3 pc. Figure 1 is a reproduction of part of the blue *Palomar Sky Survey* plate of this star and the nebula. IC 63 has a comet–like shape, with the tail pointing away from the exciting star. The tail is clearly less bright than the "head". The other nebula of similar shape is IC 59. Witt et al. (1989) have observed strong fluorescent H_2 emission in the ultraviolet spectrum of IC 63, which indicates little foreground extinction. No such emission was seen from IC 59.

Due to the proximity of the star, the cloud is exposed to several hundred times the mean Galactic ultraviolet radiation field. Thus, IC 63 is one of the nearest ultraviolet–irradiated molecular clouds, and it is therefore a better and less confused PDR to study than the usual examples such as M 17, which is very distant and highly extinguished, and NGC 2023, which has an unfavorable geometry for viewing the interaction zone edge–on.

The aim of this work is first to derive the physical conditions in the cloud, and then to use them to determine the molecular column densities. The resulting abundances will subsequently be compared with those found in cold, dark clouds such as TMC–1 and L134N, to study the effects of the radiation field and tem-

---

Send offprint requests to: D.J. Jansen

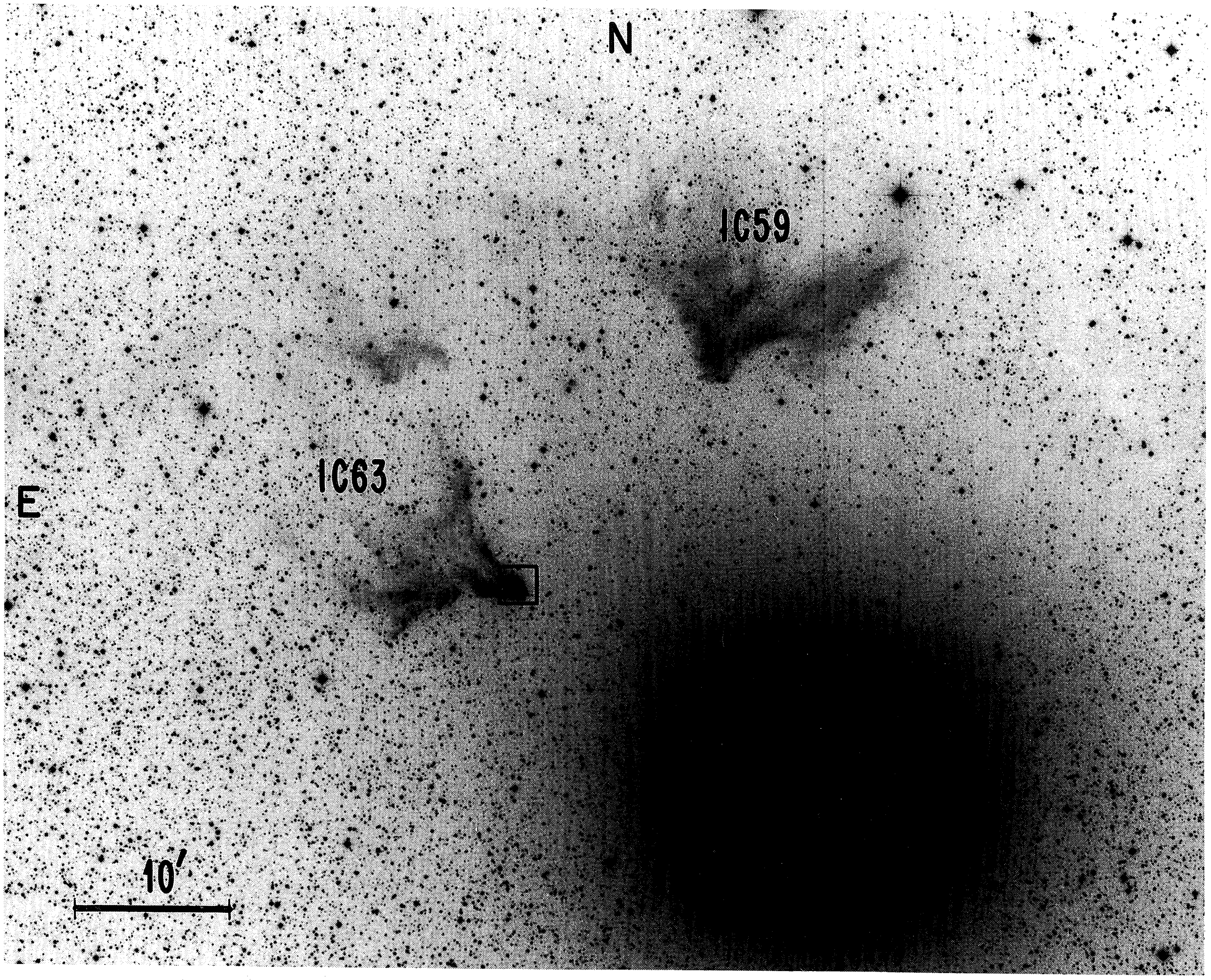

Fig. 1. Enlarged reproduction of the blue *Palomar Sky Survey* plate showing the nebula IC 63 with the nearby (heavily overexposed) star γ Cassiopeiae. The box indicates the small, brightest part of the nebula, studied in this paper

perature. In addition, we present observations of a selected set of molecules in the NGC 2023 nebula for comparison with IC 63. Preliminary results were presented in Jansen et al. (1992).

2. Observations

We have observed IC 63 in the millimeter and submillimeter range using the CSO[1] 10.4 meter telescope at Mauna Kea, U.S.A., in October 1989, November 1990 and December 1991, the NRAO[2] 12 meter telescope at Kitt Peak, U.S.A., in May 1990 and December 1992, and the IRAM[3] 30 meter telescope at Pico Veleta, Spain, in May 1991 and April 1992. A single spectrum of HCO^+ $J = 4 \rightarrow 3$ has been obtained using the JCMT[4] 15 meter telescope at Mauna Kea in July 1992. Observations of the (sub-)millimeter continuum emission were made with this telescope in May 1993 at 450, 800 and 1100 μm. Table 1 summarizes the beam sizes, main–beam efficiencies ($\eta_{\rm MB}$), spectral resolution and typical system noise temperatures for the telescopes at the observed frequencies. Note that the IRAM beam at 100 GHz is comparable to the CSO beam at 230 and 345 GHz, but that the Kitt Peak beam at 100 GHz is significantly larger.

---

[1] The Caltech Submillimeter Observatory is operated by the California Institute of Technology under funding from the U.S. National Science Foundation by contract AST 90–15755.

[2] The National Radio Astronomical Observatory is operated by Associated Universities, Inc., under contract with the U.S. National Science Foundation.

[3] Institut de Radio Astronomie Millimétrique.

[4] The James Clerk Maxwell Telescope is operated by the Royal Observatory, Edinburgh, on behalf of the UK Science and Engineering Research Council, the Netherlands Organization for Pure Research and the National Research Council of Canada.

Table 1. Telescope, receiver and backend properties

Telescope	d (m)	ν (GHz)	Beam (″)	$\eta_{\rm MB}$	$T_{\rm sys}$ (K)	Resolution (MHz)
CSO	10.4	230	30	0.72	750	0.1 or 0.5
		345	20	0.60	750	0.1 or 0.5
IRAM	30	90	26	0.67	350	0.1
		140	17	0.64	450	0.1 or 0.6
		230	13	0.52	930	0.6
		265	11	0.52	950	0.1
NRAO	12	100	63	0.91	500	0.1
		140	45	0.85	250	0.1
JCMT	15	230	22	0.60	900	0.2
		345	15	0.50	850	0.2

Pointing was regularly checked on the available planets, and should be accurate to about 5″ at the CSO, IRAM and JCMT, and 10″ at Kitt Peak. However, excursions up to twice these values were encountered during the runs.

All data were obtained in position–switching mode. The reference position was taken to be either the direction of γ Cas, which is known from ultraviolet absorption spectra to contain few foreground molecules (Ferlet et al. 1980), or a position 15′ offset in azimuth. The chopper wheel method was used to correct for atmospheric losses, giving the intensity in terms of the antenna temperature T_A^* for the CSO, IRAM and JCMT data. The main–beam temperature was calculated from this as $T_{\rm MB} = T_A^*/\eta_{\rm MB}$. The NRAO 12 m data are obtained as $T_{\rm R}^*$, and the appropriate efficiency for small sources is used to obtain $T_{\rm MB}$. Effects of possible beam–dilution are discussed later in the paper.

To investigate the calibration uncertainties, we have observed a number of lines more than once, either with the same telescope or with different telescopes. As can be seen from the data presented in Table 3, the integrated intensities generally agree to better than 30%, but the values of the peak antenna temperature and the line width can differ significantly. This is mainly due to the fact that the lines are very narrow, $\Delta V \approx 1\,{\rm km\,s^{-1}}$, and thus not always resolved in frequency. Therefore, in general the integrated intensities have been used in the analysis.

Observations of the reflection nebula NGC 2023 were made with the CSO in November 1990, the JCMT in January 1992, and the IRAM telescope in April 1992, at the position 80″ south of the illuminating star HD 37903 where Gatley et al. (1987) observed strong fluorescent H_2 emission. The same efficiencies listed in Table 1 apply.

3. Results

3.1. Molecular maps

The IC 63 nebula was mapped in the 2 → 1 and 3 → 2 lines of ^{12}CO at the CSO. A total of 67 and 48 spectra, respectively, were obtained with typical rms noise of 0.2 K. The spacing between the positions was in both cases 15″, so that the 2 → 1 map is fully sampled, whereas the 3 → 2 map is only slightly undersampled. The contour maps based on these spectra are presented in Fig. 2. The (0,0) coordinate of the map refers to the position where strong ultraviolet emission of H_2 has been found, $\alpha(1950) = 00^h55^m58^s$, $\delta(1950) = +60°37'07''$. Smaller maps, of 9 spectra each, were obtained at IRAM in the 2 → 1 lines of ^{13}CO and CS with 20″ spacing, so these maps are also slightly undersampled.

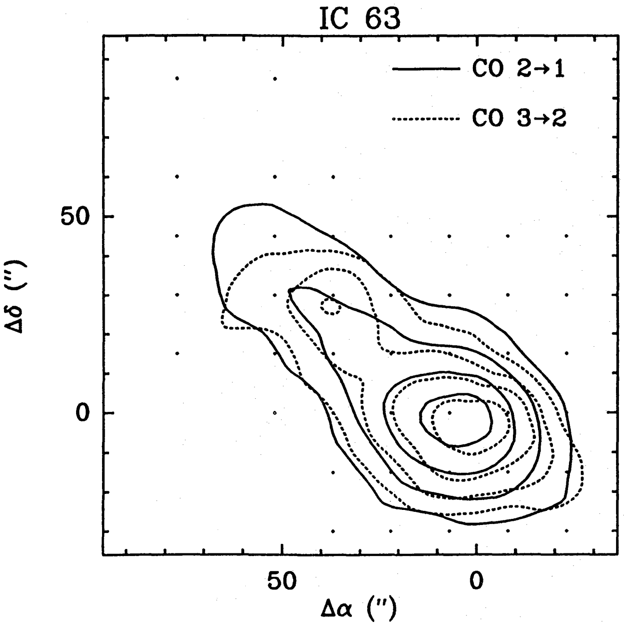

Fig. 2. Map of ^{12}CO in the region indicated by the box in Fig. 1 obtained at the CSO. Solid contours are the $J = 2 \to 1$ integrated emission and dashed contours the $J = 3 \to 2$ integrated emission $\int T_{\rm MB} dV$. In both cases, contours are at 30, 50, 70 and 90% of the maximum emission of 33 K km s^{-1} and 38 K km s^{-1}, respectively. The (0,0) of the map is at $\alpha(1950) = 00^h55^m58^s$, $\delta(1950) = 60°37'07''$. The illuminating star γ Cas is at $(-16'.95, -10'.33)$

It is seen that the molecular emission arises from a small, elongated part of the nebula, less than 1′ × 2′ in size. The major axis of the cloud points towards γ Cas, giving the impression of a banner straining in the wind (and radiation) that emanates from the star. The two maps are remarkably similar and have peak main–beam temperatures of $T_{\rm MB}$ = 23.3 and 23.7 K in the CO 2 → 1 and 3 → 2 lines, respectively, at the (0,0) position. The fact that the strongest lines coincide with the brightest nebulosity and with the H_2 fluorescent emission assures that the molecular cloud is associated with IC 63 and that it is at virtually the same distance from us as γ Cas. The strongest CO emission originates in a very small area with a FWHM size of $\Delta\alpha \approx 40''$ and $\Delta\delta \approx 20''$, as derived from the highest resolution 3 → 2 map, deconvolved for the 20″ beam. At the distance of IC 63 (230 pc), this angular size is equivalent to 0.04 pc × 0.02 pc.

The IRAM ^{13}CO 2 → 1 and CS 2 → 1 maps are consistent with this source size, although they do not contain sufficient data points for an independent determination. The CS map suggests that the densest part of the source, where most of the molecular emission arises, is smaller and less elongated than the ^{12}CO emission. We therefore adopted a source size of $30'' \times 20''$ in order to correct the observations of molecules other than ^{12}CO for beam dilution. The CO 2 → 1/3 → 2 peak intensity ratio appears almost constant over the map, which suggests that the kinetic temperature and density do not vary much over the whole region. The decrease in antenna temperatures towards the boundary can be explained by a decrease in column density.

The CO line profiles are narrow, $\Delta V \approx 1.5\,\mathrm{km\,s^{-1}}$ or less, which indicates that there cannot be a significant shocked component. The line emission peaks at a radial velocity $V_{LSR} \approx 0.6$ km s^{-1} with respect to the local standard of rest, with a shift towards slightly higher velocity, $V_{LSR} \approx 1.6$ km s^{-1}, at the north–east side of the cloud. The profiles also show a weak, broader underlying component in that direction with $\Delta V \approx 2-3\,\mathrm{km\,s^{-1}}$.

Some CO 2 → 1 spectra were also taken in the direction of IC 59. At the position listed by Witt et al. (1989), the resulting $T_A^* = 2.2\,\mathrm{K}$ is only about one tenth of that observed in IC 63. Because the ^{12}CO lines in IC 63 have optical depths $\tau \geq 1$ (see Sect. 4.2), the amount of molecular material in IC 59 is less than one tenth of that present in IC 63. Moreover, the CO emission occurs at a velocity $V_{\mathrm{LSR}} = -20.6\,\mathrm{km\,s^{-1}}$, and appears extended over more than $10'$. This is significantly larger than the optical nebulosity, so that it is unlikely that this material is associated with the nebula. We have therefore not searched for any other molecules in IC 59. The absence of molecules in IC 59 is consistent with the fact that Witt et al. (1989) detected neither H_2 fluorescence nor "extended red emission" there.

3.2. *IRAS maps and submillimeter fluxes*

The IC 63 nebula can also be traced by far–infrared emission from dust. In Fig. 3, the IRAS images at 100, 60, 25 and 12μm are presented, processed as described by Wesselius et al. (1988)[5]. The IC 63 and IC 59 nebulae are clearly visible in the 100 and 60μm maps, whereas the star γ Cas shows up most strongly at 12μm. The feature midway between IC 63 and IC 59 appears to be an unrelated object, with a very different far–infrared spectrum. It also has no associated CO emission around $V_{LSR} \approx 0$ km s^{-1}. The shapes of IC 63 and IC 59 at 100μm are similar to those seen in the optical picture (Fig. 1), but the angular resolution of the IRAS data is too low to allow a detailed comparison with the CO map. Table 2 lists the measured peak surface brightness and integrated fluxes in excess of background for IC 63, IC 59, γ Cas and the unidentified object. The visible nebulosity of IC 63 is approximately $90''$ in diameter, i.e. several times larger than the molecular source. In arriving at the tabulated fluxes for this source, we have adopted the effective beam solid angles for IRAS and have assumed a source size of $20'' \times 30''$. These fluxes at 60 and 100 μm are approximately 20–40% larger than those listed in the IRAS Point Source Catalog for source 00560+6037. The fluxes derived from the maps for IC 59 and the unidentified source make no allowance for source extent. For IC 59 this flux at 100 μm is 40% larger than the tabulated point–source flux of 00547+6052. The 60/100 μm flux ratio of IC 63 is somewhat higher than that of IC 59, while that of the unidentified source is higher than for either reflection nebula. The fluxes listed in Table 2 imply an infrared luminosity of IC 63, $L_{\mathrm{IR}} = 7.3(D/230)^2\,\mathrm{L}_\odot$, for the wavelength range $\lambda = 8-400$ μm, based upon the formula of Deutsch & Willner (1987).

Emission at submillimeter wavelengths was detected from IC 63 in a much smaller aperture ($< 20''$) using the JCMT. The measured fluxes are : 900 ± 150 mJy/beam at 450μm ($17.5''$ beam), 98 ± 15 mJy/beam at 800μm ($16.8''$ beam) and 15 ± 8 mJy/beam at 1100μm ($18.5''$ beam). Note that the measured intensity at 1100 μm is less than 1% of the intensity of the 2.7 K cosmic background radiation and is thus rather uncertain.

3.3. *Molecular spectra*

Apart from the maps, many other molecular lines were observed only at the (0,0) map position that corresponds to the peak CO 2 → 1 emission of IC 63. Figure 4 shows examples of the spectra. All lines could be fitted well by single Gaussians, and the parameters of these fits are presented in Table 3. The listed values are the antenna temperature T_{MB} corrected for beam efficiency, the linewidth ΔV and the integrated intensity $W = \int T_{\mathrm{MB}} dV$ in K km s^{-1}. Since not all lines are fully resolved, the line widths may appear significantly larger than $\Delta V \approx 1\,\mathrm{km\,s^{-1}}$. In these cases, which are marked by an asterisk in the table, T_{MB} and ΔV should not be trusted, but $\int T_{\mathrm{MB}} dV$ will still be correct.

Table 3 shows that in general the measured intensities at the various telescopes are consistent within 30%. A major exception is formed by the Kitt Peak observations, which are usually much lower than the corresponding IRAM data, as illustrated by the HCO$^+$ 1 → 0 and CS 2 → 1 lines. Since the Kitt Peak data refer to a much larger beam of about $60''$, the apparent discrepancy is mostly caused by beam dilution. As discussed in Sect. 3.1, the size of the compact molecular source was found to be about $30'' \times 20''$. The source is therefore marginally resolved by the CSO at 345 GHz, where the beam size is about $20''$, and at IRAM, where the beam is $< 25''$. However, the source fills only 23% of the Kitt Peak beam at 115 GHz, and about 50% of the CSO beam at 230 GHz. The main–beam temperatures were thus corrected for the effects of beam dilution for comparison with models. The corrected radiation temperatures are denoted as T_{R}, and are related to T_{MB} by $T_{\mathrm{R}} = T_{\mathrm{MB}}(1 + \Omega_B/\Omega_S)$, where Ω_B and Ω_S are the solid angles subtended by the beam and the true source size, respectively. For ^{12}CO, the source size was found to be about 1500 arcsec^2 from the 2–1 map, whereas for the other molecules, it was taken to be 600 arcsec^2. For this source size, the CS 2–1, HCO$^+$ 1–0, HCN 1–0 and HNC 1–0 Kitt Peak and IRAM data are in very good agreement. However,

---

[5] The IRAS data have been processed using the GEISHA analysis system developed by the Laboratory for Space Research at Groningen, The Netherlands. This development was partly funded by the University of Groningen, the Space Science Department of ESTeC, and the Air Force Geophysics Laboratory (U.S.A.).

Table 2. IRAS fluxes

	RA (1950.0)	Dec (1950.0)	Peak surface brightness (MJy sr^{-1})				Color corrected flux^a (Jy)			
			12 μm	25 μm	60 μm	100 μm	12 μm	25 μm	60 μm	100 μm
IC 63^b	$0^h55^m58^s$	60°37′	8.0	9.7	86	101	2.57	2.73	56	105
IC 59	$0^h54^m40^s$	60°49′	5.0	3.7	47	94	4.52	4.06	39	119
γ Cas	$0^h53^m40^s$	60°27′	34.8	17.0	21	33	7.69	1.83	...	...
Unidentified object	$0^h55^m30^s$	60°48′	10.8	54.1	149	115	3.55	8.45	59	131
Background^c	$0^h55^m58^s$	60°12′	0.0	0.0	8	23	...	...	...	...
Beam area Ω_B (10^{-7} sr)			2.8	3.1	6.5	13.				

^{a} These fluxes have been background–subtracted and color–corrected. ^{b} IC 63 fluxes assume the IRAS beam areas and a 20″ × 30″ source. ^{c} Background measured at a position 25′ south of IC 63.

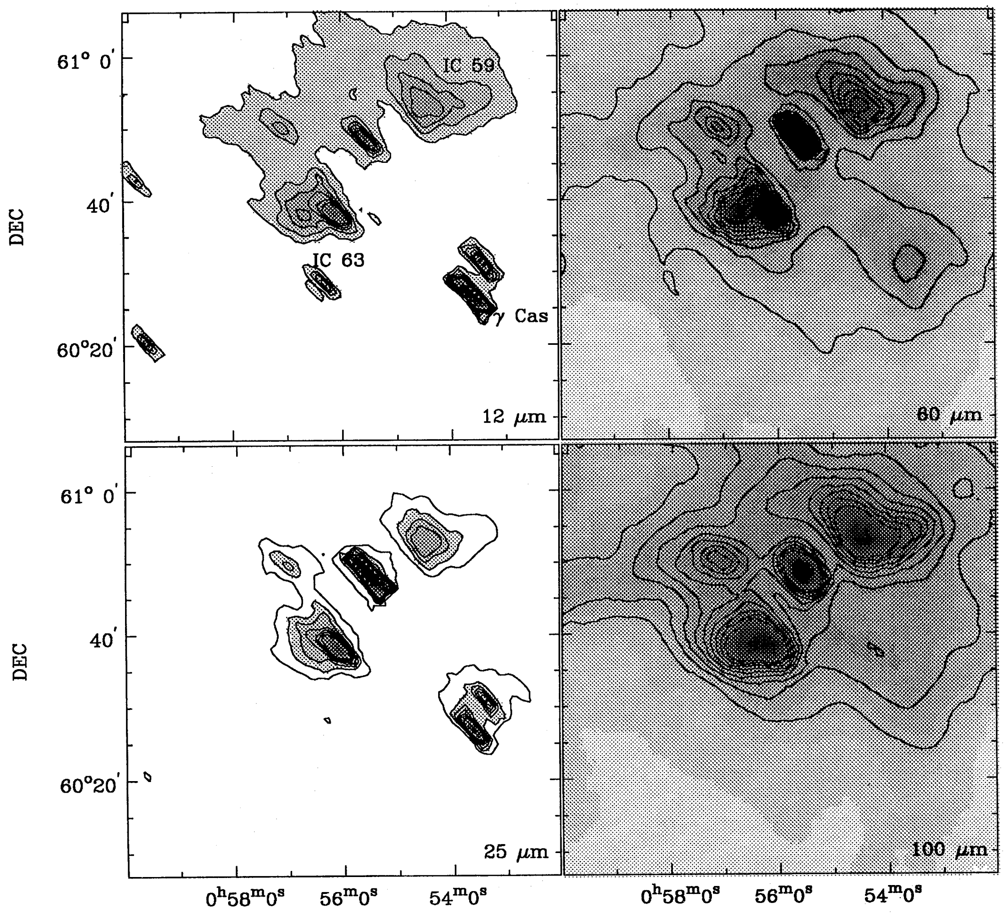

Fig. 3. IRAS maps of the region around IC 63. (a) 12μm: contour levels are in steps of 1 MJy sr^{-1}, starting at 1 MJy sr^{-1}. (b) 25μm: contour levels are in steps of 1 MJy sr^{-1}, starting at 1 MJy sr^{-1}. (c) 60μm: contour levels are in steps of 5 MJy sr^{-1}, starting at 10 MJy sr^{-1}. (d) 100μm: contour levels are in steps of 5 MJy sr^{-1}, starting at 30 MJy sr^{-1}

comparison of the H_2CO NRAO and IRAM data at 140 GHz and the CSO and IRAM data at 225 GHz suggest that the emission from this molecule is at least as extended as that of ^{12}CO.

4. Physical parameters

4.1. Method

In order to derive the physical parameters such as temperature and density from the observations, statistical equilibrium excitation calculations were used to fit the observations. Spontaneous and stimulated radiative processes, as well as collisional excitation and de–excitation, were included in the calculations of the level populations. The radiative transfer is approximated through a mean escape probability β, which depends only on the optical depth at line center τ:

$$\beta = \frac{3}{4\tau}\left(1 - \frac{1}{2\tau^2} + \left(\frac{1}{\tau} + \frac{1}{2\tau^2}\right)e^{-2\tau}\right), \qquad (1)$$

where the cloud is assumed to be spherically symmetric and homogeneous (Osterbrock 1989, Appendix 2). For small values of the optical depth, this formula was approximated by

Table 3. Observations and Gaussian fit parameters : IC 63

Species	Transition	ν (MHz)	$T_{\rm MB}$ (K)	ΔV (km s^{-1})	$\int T_{\rm MB} dV$ (K km s^{-1})	Telescope	Beam ($''$)	Resolution (MHz)	rms[a] (K)
CO	$1 \rightarrow 0$	115271	10.8	1.14	13.1	NRAO	54	0.1	0.09
	$2 \rightarrow 1$	230538	23.3	1.33	33.1	CSO 89	31	0.1	0.50
	$2 \rightarrow 1$	230538	16.0	1.8*	30.8	CSO 90	31	0.1	0.23
	$3 \rightarrow 2$	345796	23.7	1.52	38.2	CSO 89	21	0.1	0.35
^{13}CO	$1 \rightarrow 0$	110201	0.39	0.82	0.34	NRAO	57	0.1	0.05
	$2 \rightarrow 1$	220399	1.64	1.14	2.08	CSO 90	33	0.1	0.07
	$2 \rightarrow 1$	220399	5.97	0.74	4.71	IRAM 92	11	0.1	0.05
C^{18}O	$1 \rightarrow 0$	109782	0.10	0.57	0.06	NRAO	57	0.1	0.03
	$2 \rightarrow 1$	219560	<0.6	...	...	IRAM 92	11	1.0	0.30
CS	$2 \rightarrow 1$	97981	0.21	1.03	0.23	NRAO	64	0.1	0.04
	$2 \rightarrow 1$	97981	0.80	0.95	0.80	IRAM 91	26	0.1	0.08
	$2 \rightarrow 1$	97981	0.72	0.69	0.53	IRAM 92	26	0.1	0.06
	$3 \rightarrow 2$	146969	0.20	2.9*	0.60	IRAM 91	17	0.6	0.07
	$5 \rightarrow 4$	244936	<0.07	...	<0.36	CSO 90	29	0.1	0.04
	$5 \rightarrow 4$	244936	<0.40	...	...	IRAM 91	10	0.1	0.20
CN	$1_{\frac{3}{2},\frac{5}{2}} \rightarrow 0_{\frac{1}{2},\frac{3}{2}}$	113491	0.54	0.73	0.42	NRAO	55	0.1	0.05
	$1_{\frac{1}{2},\frac{3}{2}} \rightarrow 0_{\frac{1}{2},\frac{3}{2}}$	113191	0.28	0.69	0.20	NRAO	55	0.1	0.05
	$2_{\frac{5}{2},\frac{7}{2}} \rightarrow 1_{\frac{3}{2},\frac{5}{2}}$	226875	0.39	0.81	0.33	CSO 91	32	0.1	0.09
	$2_{\frac{5}{2},\frac{3}{2}} \rightarrow 1_{\frac{3}{2},\frac{1}{2}}$	226876	0.25	1.0	0.26	CSO 91	32	0.1	0.09
	$2_{\frac{5}{2},\frac{5}{2}} \rightarrow 1_{\frac{3}{2},\frac{3}{2}}$	226874	0.31	0.96	0.32	CSO 91	32	0.1	0.09
HCN	$1,1 \rightarrow 0,1$	88630	0.16	1.06	0.17	NRAO	70	0.1	0.03
	$1,2 \rightarrow 0,1$	88632	0.32	1.13	0.34	NRAO	70	0.1	0.03
	$1,0 \rightarrow 0,1$	88634	0.08	1.73*	0.15	NRAO	70	0.1	0.03
	$1,1 \rightarrow 0,1$	88630	0.62	1.02	0.68	IRAM 92	28	0.1	0.09
	$1,2 \rightarrow 0,1$	88632	1.24	1.03	1.37	IRAM 92	28	0.1	0.09
	$1,0 \rightarrow 0,1$	88634	0.28	1.03	0.30	IRAM 92	28	0.1	0.09
	$3 \rightarrow 2$	265886	<0.28	...	...	CSO 90	27	0.1	0.14
HNC	$1 \rightarrow 0$	90664	0.22	1.2	0.29	NRAO	69	0.1	0.04
	$1 \rightarrow 0$	90664	0.89	1.11	1.06	IRAM 92	28	0.1	0.04
HCO$^+$	$1 \rightarrow 0$	89189	0.44	2.0*	0.94	NRAO	70	0.1	0.08
	$1 \rightarrow 0$	89189	3.14	1.2	3.92	IRAM 91	28	0.1	0.07
	$3 \rightarrow 2$	267558	0.35	2.2*	0.81	CSO 90	27	0.5	0.10
	$4 \rightarrow 3$	356734	0.38	0.87	0.37	JCMT 92	14	0.2	0.10
H$_2$CO	$2_{1,1} \rightarrow 1_{1,0}$	150498	0.14	1.6*	0.23	IRAM 91	17	0.6	0.06
	$2_{1,2} \rightarrow 1_{1,1}$	140840	0.38	1.0	0.41	IRAM 91	18	0.1	0.07
	$2_{1,2} \rightarrow 1_{1,1}$	140840	0.25	1.0	0.27	NRAO	45	0.1	0.03
	$3_{0,3} \rightarrow 2_{0,2}$	218222	<0.08	...	...	CSO 91	33	1.0	0.04
	$3_{1,2} \rightarrow 2_{1,1}$	225698	0.18	0.86	0.18	CSO 90	32	0.1	0.08
	$3_{1,2} \rightarrow 2_{1,1}$	225698	0.11	1.6*	0.19	IRAM 92	11	0.6	0.05
	$3_{2,1} \rightarrow 2_{2,0}$	218760	<0.24	...	...	IRAM 91	11	0.6	0.12
	$3_{2,2} \rightarrow 2_{2,1}$	218476	<0.24	...	...	IRAM 91	11	0.6	0.12
	$3_{2,2} \rightarrow 2_{2,1}$	218476	<0.08	...	...	CSO 91	33	1.0	0.04
CH$_3$OH	$2 \rightarrow 1$	96741	<0.14	...	...	IRAM 91	26	0.1	0.07
C$_2$H	$1_{2,1} \rightarrow 0_{1,0}$	87329	0.37	1.12	0.45	IRAM 92	29	0.1	0.08
N$_2$H$^+$	$1_2 \rightarrow 0_1$	93174	0.09	0.65	0.13	IRAM 92	27	0.1	0.04
	$1_1 \rightarrow 0_1$	93172	<0.07	...	...	IRAM 92	27	0.1	0.04
	$1_0 \rightarrow 0_1$	93176	<0.07	...	...	IRAM 92	27	0.1	0.04
HC$_3$N	$11 \rightarrow 10$	100076	<0.10	...	...	NRAO	63	0.1	0.05
CH$_3$CN	$8_K \rightarrow 7_K$	147172	<0.12	...	...	IRAM 91	17	0.6	0.06
HNCO	$6_{0,6} \rightarrow 5_{0,5}$	131886	<0.15	...	...	IRAM 92	19	0.1	0.07
H$_2$S	$1_{1,0} \rightarrow 1_{0,1}$	168763	0.72	0.58	0.44	IRAM 92	15	0.1	0.09
SO	$2_2 \rightarrow 1_1$	86094	<0.06	...	...	IRAM 92	29	0.1	0.03
	$3_2 \rightarrow 2_1$	99300	<0.12	...	...	NRAO	63	0.1	0.06
SO$_2$	$5_{2,4} \rightarrow 4_{1,3}$	241616	<0.20	...	...	IRAM 91	10	0.1	0.10
SiO	$3 \rightarrow 2$	130268	<0.10	...	...	IRAM 92	19	0.1	0.05

All upper limits are 2σ; An asterisk marks the observations where the line is unresolved and the profile is thus dominated by instrumental broadening. [a] rms noise per resolution element

1994A&A...282..605J

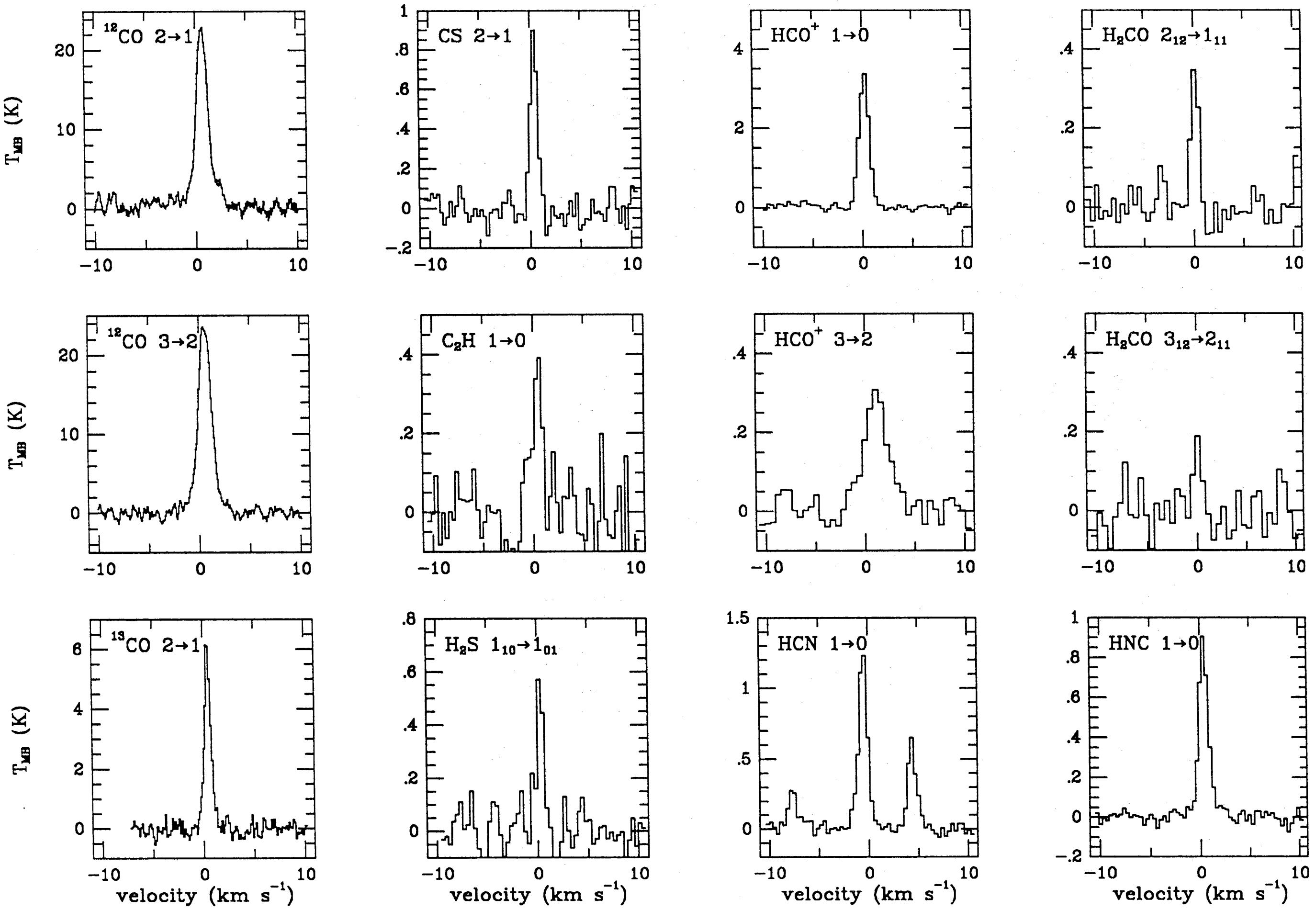

Fig. 4. Examples of spectra of IC 63 taken at the various telescopes, converted to $T_{\rm MB}$–scale. The ^{12}CO 2→1, 3→2, ^{13}CO 2→1, HCO$^+$ 3→2 and H$_2$CO $3_{12} \rightarrow 2_{11}$ spectra were taken at the CSO, the remaining spectra at the IRAM 30m. Note that the HCO$^+$ 3→2 spectrum was taken with the low–resolution (0.5 MHz) backend

$$\beta = 1 - \frac{3}{4}\tau + \frac{2}{5}\tau^2 - \frac{1}{6}\tau^3 + \frac{2}{35}\tau^4 + \mathcal{O}(\tau^5), \tag{2}$$

which is the fourth order series–expansion of Eq. 1. The optical depth of transition $u \rightarrow l$ is related to the level populations through

$$\tau = \frac{A_{ul}}{8\pi\tilde{\nu}^3}\frac{N}{1.065\Delta V}\left[x_l\frac{g_u}{g_l} - x_u\right], \tag{3}$$

where A_{ul} is the spontaneous transition probability in s^{-1}, $\tilde{\nu} = \nu/c$ the transition frequency in cm^{-1}, N the total column density of the molecule in cm^{-2}, x_i the fractional population of level i, and g_i the corresponding statistical weight. The line is presumed to have a Gaussian profile with FWHM ΔV in cm s^{-1}. Because the cloud is warm (see below), most lines have small optical depths, the major exception being ^{12}CO. Note however that even when the lines are optically thick, our excitation analysis includes the optical depth effects explicitly.

Collisional (de)excitation can occur with molecular hydrogen and with free electrons. Collisions with atomic hydrogen and helium are not taken into account explicitly. However, the electrons are quite important in exciting polar molecules (electric dipole moments $\mu \geq 1$ D) when the electron fraction becomes larger than 1×10^{-5} (cf. Drdla et al. 1989), which might well be the case in a PDR like IC 63. Rates for collisions with electrons were computed according to the approximation of Dickinson & Flower (1981) and Dickinson et al. (1977). Table 4 lists the references to the adopted neutral collision rates. In the case of HCN, scaled helium cross sections were used, since para-H$_2$ in its lowest rotational state (J = 0) is a "structureless" particle, like the helium atom. The same collision rates were adopted for HNC, whose dipole moment is nearly equal to that of HCN. No collision rates are available for C$_2$H, so that again the HCN rates were used, scaled by the difference in reduced mass. Preliminary calculations of SO excitation simply assume a collision rate of 2×10^{-11} cm^3 s^{-1} for the $(J, N) = (1, 0) \rightarrow (0, 1)$ transition and adopt rates that scale with radiative line strengths for all other dipole–allowed transitions. The spontaneous emission probabilities were computed using the dipole moments listed in Table 5. The ambient radiation field was taken to be the cosmic background field represented by a blackbody with $T_{\rm BG}$ = 2.73 K. Other radiation fields were found to be unimportant for the

Table 4. Collisional cross sections

Species	Collision partner	Reference
CO	H_2	Schinke et al. (1985)
CS	H_2	Green (priv. comm., cf Turner et al. 1992)
CN	H_2	from CS rates (Green & Chapman 1978; see Black & van Dishoeck 1991)
HCO^+	H_2	Green (1975), Monteiro (1985)
HCN	He	Green & Thaddeus (1974)
(hfs)		Monteiro & Stutzki (1986)
H_2CO	H_2	Green (1991)
N_2H^+	H_2	Green (1975)
HNCO	He	S. Green, unpublished results
CH_3CN	H_2	Green (1986)
SiO	H_2	Green (priv. comm., cf Turner et al. 1992)

Table 5. Dipole moments

Species	μ (Debye)
CO	0.112
CS	1.96
CN	1.45
HCN	2.98
HNC	2.7
HCO^+	3.91
H_2CO	2.331
CH_3OH	0.885 (μ_a)
C_2H	0.8
N_2H^+	3.4
HC_3N	3.6
CH_3CN	3.92
HNCO	1.575 (μ_a)
H_2S	0.97
SO	1.52
SO_2	1.635
SiO	3.1

species considered here, since small heavy molecules like CO have their lowest transitions near the peak of the cosmic background radiation. A model of the thermal dust emission was constructed to fit the IRAS fluxes at 60 and 100μm and the submillimeter continuum measurements. Even if the far-infrared source is as compact as the $20'' \times 30''$ molecular core, the internal continuum radiation temperature (including the cosmic background) is less than 3.25 K at $\nu \leq 400$ GHz.

The other input parameters to the excitation calculation are the kinetic temperature of the gas, the density of the collision partner(s), the total column density of the molecule and the line width. These physical input parameters were varied until agreement between the computed Rayleigh–Jeans equivalent radiation temperatures and the observed values were found. The procedure was as follows. First, the temperature and density were determined independently of the abundances: the relative strengths of the lines depend only on these parameters but not on column density, as long as the lines are optically thin. Second, given these physical parameters, the column densities were adjusted to fit the absolute intensities.

4.2. Determination of temperature and density

The primary temperature diagnostic in our IC 63 data is the $^{12}C^{16}O$ molecule. The $2 \rightarrow 1$ radiation temperature is T_R = 35 K, corrected for beam dilution of a source of solid angle Ω_S = 1500 arcsec^2. This radiation temperature is related to the excitation temperature $T_{\rm ex}$ by

$$2k\tilde{\nu}^2 T_{\rm R} = \Big(B_\nu(T_{\rm ex}) - B_\nu(T_{\rm BG})\Big)\left(1 - e^{-\tau}\right) \qquad (4)$$

where $B_\nu(T)$ is the Planck function and k is Boltzmann's constant. For $\tau(2 \rightarrow 1) >> 1$, $T_{\rm ex}$ = 40.5 K. This provides a lower limit on the kinetic temperature. Detailed excitation calculations provide a good representation of the three observed ^{12}CO lines with a somewhat higher kinetic temperature, $T \approx 50$ K, and $\tau(2 \rightarrow 1) \approx 4$. That analysis is sensitive to the $2 \rightarrow 1/1 \rightarrow 0$ intensity ratio, which in turn is sensitive to the correction for beam dilution, especially for the $1 \rightarrow 0$ line. Within the various uncertainties, the mean kinetic temperature is constrained within approximately 20%; therefore, we adopt $T = 50 \pm 10$ K. This temperature refers to the region from which the optically thick ^{12}CO emission arises, and is therefore not necessarily the temperature representative of all the molecular material. The effects of a possible temperature gradient will be discussed in Sect. 5.4.

The density can be inferred from ratios of lines of molecules with larger dipole moments. The best examples are provided by HCO^+, CS, HCN and H_2CO, for which several lines have been observed, and for which collisional cross sections are available so that an excitation analysis can be performed. Figure 5 shows the relevant line ratios as functions of temperature and molecular hydrogen density. The column densities used in this figure are close to those which will be inferred in Sect. 5, about 10^{13} cm^{-2}. For such column densities, most lines are optically thin, except at the lowest frequencies for low temperatures $T < 40$ K. Since IC 63 is a PDR, the density of free electrons is expected to be higher than in dark molecular clouds. Models suggest that the electron fraction $x(e) = n(e)/n(H_2)$ may be as high as $10^{-5} - 10^{-4}$, in which case electron excitation competes effectively with the neutral excitation (Drdla et al. 1989). Since the electron collisions obey different selection rules from neutral impact ($\Delta J = \pm 1$ transitions are generally favored), the line ratios may be altered. Figure 5 refers to an electron fraction of 10^{-4}. For comparison, Fig. 6 shows these line ratios for x(e)=10^{-5}. It is seen that in general a high electron fraction favors the excitation of the higher J levels.

Since the narrow spectral lines are not always resolved, we have used the integrated radiation temperature W[K km s^{-1}] for comparison with the modeling. In case of upper limits, we assumed a linewidth of 1 km s^{-1} in order to convert them to limits on the integrated intensity. The resulting observed line ratios corrected for beam dilution are: HCO^+ $1 \rightarrow 0/3 \rightarrow 2 \approx 5.1 \pm 1.5$, HCN $1 \rightarrow 0/3 \rightarrow 2 > 8$, H_2CO $2_{12} \rightarrow 1_{11}/$

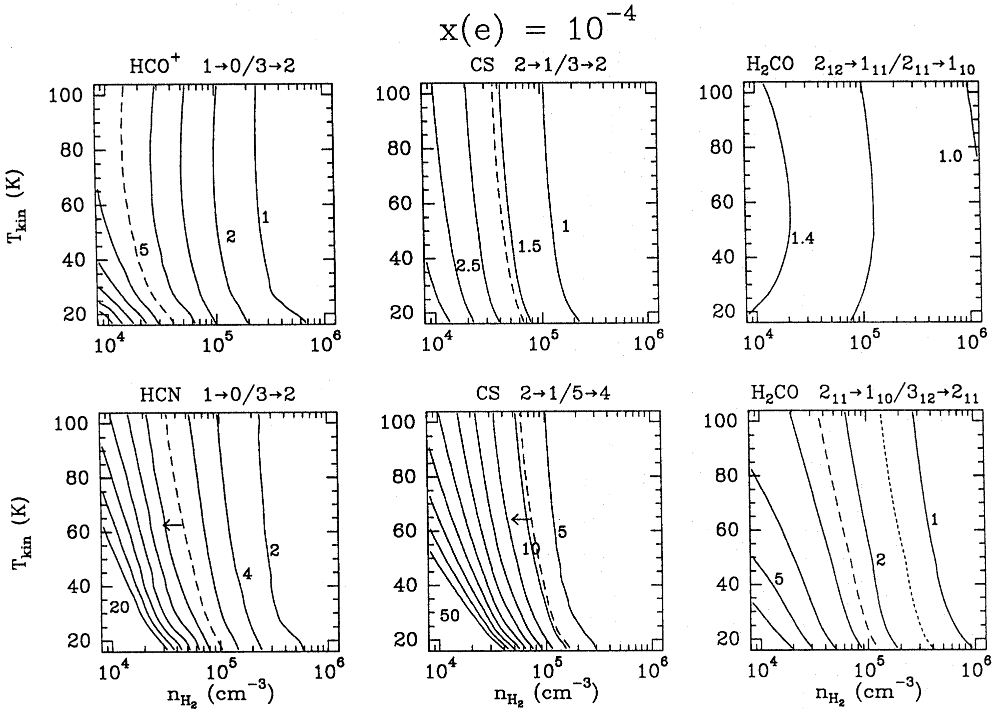

Fig. 5. Calculated line ratios of (a) HCO^+ 1 → 0/3 → 2, (b) HCN 1 → 0/3 → 2, (c) CS 2 → 1/3 → 2, (d) CS 2 → 1/5 → 4, (e) H_2CO $2_{12} \rightarrow 1_{11}/2_{11} \rightarrow 1_{10}$ and (f) H_2CO $2_{11} \rightarrow 1_{10}/3_{12} \rightarrow 2_{11}$ as functions of temperature and density. The contour levels range from: (a) 1 – 10 in steps of 1; (b) 1 – 15 in steps of 1; (c) 1 – 3 in steps of 0.5 ; (d) 2.5,5,...,25, in steps of 2.5; (e) 1.0–1.4 in steps of 0.2; (f) 1 – 6 in steps of 1. All curves refer to an electron fraction $x(e) = n(e)/n(H_2) = 10^{-4}$. The adopted column density is 1×10^{13} cm^{-2} for each molecule, and the line width ΔV=1 km s^{-1}. The long-dashed lines indicate the ratios found from observations. The short-dashed line in the lower right panel is the value obtained using the CSO observation at 225 GHz

$3_{12} \rightarrow 2_{11} \approx 2.5 \pm 1$, CS 2 → 1/3 → 2 ≈ 1.6 ± 0.5 and CS 2 → 1/5 → 4 > 8. In the case of the HCN 1 → 0 transition, the sum of the three hyperfine structure components was used for comparison with the 3 → 2 data, since these components are not separately observable in the latter case. The observed line ratios are indicated by dashed lines in Figs. 5 and 6. It is seen that for $T \approx$40–60 K, the ratios are consistent with $n(H_2) \approx (5 \pm 2) \times 10^4$ cm^{-3}. This estimate of the density is not altered much if part of the gas is at somewhat lower temperatures, $T \approx$ 20–40 K. The analysis of the ^{12}CO lines yields a best–fitting H_2 density in harmony with this value. The H_2CO $2_{12} \rightarrow 1_{11}/3_{12} \rightarrow 2_{11}$ ratio is also in agreement with this density if the IRAM measurement of the $3_{12} \rightarrow 2_{11}$ line is used (long-dashed line in Figs. 5 and 6). The CSO observation (short-dashed line) seems to indicate a higher density, but this is only a 2σ measurement. A high electron fraction favors the lower end of the inferred density range. Our marginal 3σ detection of the HCO^+ 4 → 3 line at the JCMT would fit better with the high end.

In summary, the excitation analysis shows that the average temperature and density in the cloud are :

$$T = 50 \pm 10\,\mathrm{K}, \quad n(H_2) = (5 \pm 2) \times 10^4\,\mathrm{cm}^{-3}.$$

At the adopted density, the volume of the CO–emitting region in IC 63, $(0.035 \times 0.035 \times 0.053)$ pc^3 at D = 230 pc, contains a total mass of 0.2 M$_\odot$. This estimate assumes a fully molecular cloud and an interstellar mass per H_2 molecule of 4.34×10^{-24} g, including He and heavier elements. The inferred density is significantly higher than $n(H_2) \approx 0.15$ cm^{-3} derived by Witt et al. (1989) from the H_2 ultraviolet fluorescence. However, as will be shown in a subsequent paper (see also Black & van Dishoeck 1987; Sternberg 1989; Sosin et al. 1990), the H_2 fluorescence data are better explained with a higher density ($n(H_2) \geq 1 \times 10^4$ cm^{-3}) at $T \approx 50$ K.

4.3. The infrared emission and radiative balance

As described in Sect. 3.2 and Table 2, the spectral energy distribution of IC 63 peaks in the far–infrared and indicates a luminosity $L_{IR} = 7.3(D/230)^2$ L$_\odot$, where D is the distance to IC 63 in pc. It is of interest to compare this luminosity with the radiant energy received by the nebula from γ Cas. For this purpose we use the ultraviolet spectrophotometry of Code & Meade (1979) over the wavelength range λ = 1200 – 3580 Å, the broad–band flux of Troy et al. (1975) at λ = 950 Å, and the following magnitudes: U = 1.24, B = 2.32, and V = 2.47. Gamma Cas is a peculiar Be star of type B0.5 IVpe, which is known to be variable. It was one of the first early-type stars found to have an infrared excess (Woolf et al. 1970), and is a variable X–ray source (e.g. White et al. 1982; Murakami et al. 1986). Owing to its peculiar colors, the extinction to γ Cas is difficult to determine, although a value of the color excess E_{B-V} = 0.03 mag seems to be consistent with all the data. Ignoring these complications, we estimate an extinction–corrected flux at Earth of 7.4×10^{-10} photons s^{-1} cm^{-2} Hz^{-1} at λ = 1000 Å. This implies a far–ultraviolet flux incident on the boundary of IC 63 of 2.2×10^{-5} photons s^{-1} cm^{-2} Hz^{-1} at λ = 1000 Å. This flux is 650 times that of the mean stellar background in the solar neighborhood at this wavelength as estimated by Draine (1978) and 900 times the background flux estimated by Mathis et al. (1983). If we assume that all of the ionizing photons are excluded from the neutral cloud associated with IC 63, then the integrated flux from the visible region to the Lyman limit of H incident upon the nebula is F = 0.62 ergs s^{-1} cm^{-2}. The corresponding power crossing an area that subtends the same angular diameter as the molecular cloud (600 arcsec^2) is $1.2(D/230)^2$ L$_\odot$. Thus the non–ionizing starlight is insufficient to account for the far–infrared emission of IC 63, unless the extent of the

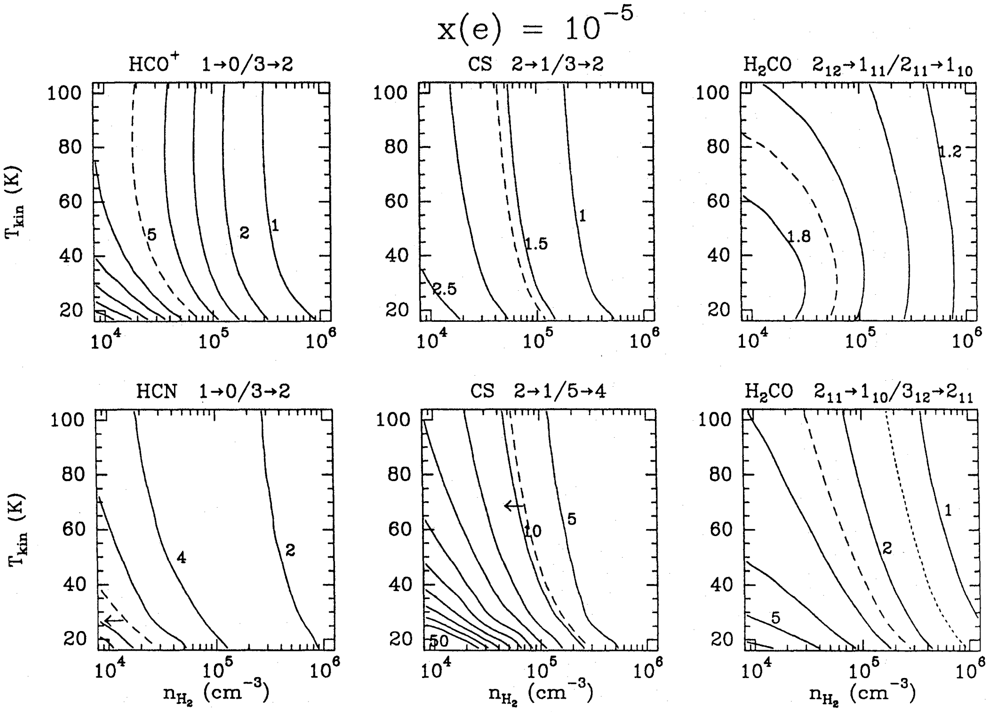

Fig. 6. As Fig. 5, but for $x(e) = 10^{-5}$

infrared emission is several times larger than that of the central molecular cloud.

If we assume that the far–infrared and submillimeter emission is thermal radiation from a single population of dust particles at temperature T_d, then the spectrum can be represented by

$$f_\nu = B_\nu(T_\mathrm{d})\left(1 - e^{-\tau_\nu}\right)\Omega_\mathrm{S}. \tag{5}$$

We use an opacity law of the form

$$\tau_\nu \propto \nu^\beta \tag{6}$$

at long wavelengths ($\lambda > 40\mu$m) that joins smoothly with the average interstellar extinction law of Becklin et al. (1978) at shorter wavelengths.

Equation (5) fits the submillimeter surface brightnesses for T_d = 45 K, $\tau_{800} = 1.2 \times 10^{-4}$ and $\beta = 2$, which is the steepest opacity function possible under normal circumstances. A lower value of β would require unrealistically high dust temperatures. If we assume that the dust emission arises mostly within the compact molecular core of size $20'' \times 30''$, then the parameters T_d = 30.5 K, $\tau_{800} = 2.8 \times 10^{-4}$, and $\beta = 2$ reproduce the 800 and 450 μm fluxes within 6% and the 100 and 60 μm fluxes within 15%. Thus the various uncertainties allow at least a factor–of–two uncertainty in the derived optical depth.

5. Column densities and abundances

5.1. Column densities of heavy molecules

Column densities are derived from the measured line intensities through the excitation analyses described above. Since collisions with electrons may play an important part in a PDR like IC 63, we considered two cases : one with $x(e) = 1 \times 10^{-4}$, where electrons are as important as molecular hydrogen, and one case with $x(e) = 1 \times 10^{-5}$, where electrons play only a marginal role. Given the physical conditions derived above from the relative line strengths, the column densities can be inferred by fitting the absolute antenna temperatures. In addition to HCO$^+$, HCN, CS and H$_2$CO, such detailed excitation calculations were also performed for CN, HNC, C$_2$H, N$_2$H$^+$, CH$_3$CN, HNCO, SO, and SiO.

For the remaining molecules, no reliable collisional cross sections are available, so that no excitation model was set up. In these cases, column densities have been derived assuming that all level populations can be characterized by a single rotational excitation temperature T_rot. Then

$$\log\left(\frac{3kW}{8\pi^3\nu S\mu^2 g_\mathrm{u}}\right) = \log\frac{N}{Q_\mathrm{rot}} - \frac{E_\mathrm{u}\log e}{kT_\mathrm{rot}} \tag{7}$$

where W is the integrated intensity, S the line strength factor of the transition, μ the dipole moment of the molecule, g_u and E_u the statistical weight and energy of the upper level, and Q_rot the value of the rotational partition function at T_rot (see Blake et al. 1987). Since only one or two lines of each molecule were observed, we do not have sufficient data to derive both T_rot and N. Since the molecules have large dipole moments (see Table 5), a rotational temperature T_rot = 10 K will be assumed, less than the kinetic temperature. The excitation calculations for other molecules with substantial dipole moments such as CS and HCN give rotation temperatures close to 10 K for the conditions appropriate to IC 63. Note that when Eq. (7) is used the details of the excitation mechanism are ignored; therefore, the electron fraction does not influence the fit and hence only one value is tabulated in Table 7.

Table 6. Radiation temperatures and model fits

Molecule	Line	W (K km s^{-1})		
		Observed[a]	Model[b] $x(e) = 10^{-4}$	Model[b] $x(e) = 10^{-5}$
CO[a]	$1 \rightarrow 0$	33.1	34.2	34.2
	$2 \rightarrow 1$	48.0	44.9	44.9
	$3 \rightarrow 2$	47.0	42.9	42.9
	$4 \rightarrow 3$	...	39.6	39.6
^{13}CO	$1 \rightarrow 0$	1.79	1.77	1.77
	$2 \rightarrow 1$	5.25	5.55	5.55
	$3 \rightarrow 2$	...	8.13	8.13
	$4 \rightarrow 3$	...	7.83	7.83
C^{18}O	$1 \rightarrow 0$	0.31	0.23	0.23
	$2 \rightarrow 1$	<0.71	0.75	0.75
	$3 \rightarrow 2$	...	1.16	1.16
	$4 \rightarrow 3$	...	1.13	1.13
CS	$2 \rightarrow 1$	1.25	1.34	1.37
	$3 \rightarrow 2$	0.80	0.78	0.75
	$5 \rightarrow 4$	<0.15	0.07	0.08
CN	$1_{\frac{3}{2},\frac{5}{2}} \rightarrow 0_{\frac{1}{2},\frac{3}{2}}$	1.85	1.87	1.88
	$1_{\frac{1}{2},\frac{3}{2}} \rightarrow 0_{\frac{1}{2},\frac{3}{2}}$	0.88	0.60	0.52
	$2_{\frac{5}{2},\frac{3}{2}} \rightarrow 1_{\frac{3}{2},\frac{1}{2}}$	0.56	0.46	0.38
	$2_{\frac{5}{2},\frac{7}{2}} \rightarrow 1_{\frac{3}{2},\frac{5}{2}}$	0.71	0.99	0.91
	$2_{\frac{5}{2},\frac{5}{2}} \rightarrow 1_{\frac{3}{2},\frac{3}{2}}$	0.65	0.71	0.61
HCN	$1,1 \rightarrow 0,1$	1.27	1.29	1.35
	$1,2 \rightarrow 0,1$	2.57	2.67	2.38
	$1,0 \rightarrow 0,1$	0.52	0.20	0.35
	$3 \rightarrow 2$	<0.53	0.25	0.73
HNC	$1 \rightarrow 0$	1.95	1.89	1.85
HCO$^+$	$1 \rightarrow 0$	7.4	5.3	5.6
	$3 \rightarrow 2$	1.45	1.62	1.52
	$4 \rightarrow 3$	0.45	0.52	0.62
H_2CO	$2_{1,1} \rightarrow 1_{1,0}$	0.30	0.32	0.35
	$2_{1,2} \rightarrow 1_{1,1}$	0.52	0.42	0.59
	$3_{1,2} \rightarrow 2_{1,1}$	0.22	0.10	0.11
	$3_{0,3} \rightarrow 2_{0,2}$	<0.09	0.06	0.07
	$3_{2,1} \rightarrow 2_{2,0}$	<0.22	0.01	0.02
	$3_{2,2} \rightarrow 2_{2,1}$	<0.09	0.01	0.02
	$1_{1,0} \rightarrow 1_{1,1}$	...	0.03	–0.10
	$2_{1,1} \rightarrow 2_{1,2}$	...	–0.004	–0.04
	$1_{0,1} \rightarrow 0_{0,0}$	...	0.21	0.35
	$2_{0,2} \rightarrow 1_{0,1}$	...	0.20	0.23
	$3_{1,3} \rightarrow 2_{1,2}$	...	0.19	0.26

[a] The tabulated $W = \int T_{\rm R} dV$ are the integrated main–beam temperatures, corrected for beam dilution. In cases of upper limits, a line width $\Delta V = 1$ km s^{-1} has been used to transform these limits to limits on the integrated main–beam temperature. The adopted source size is 1500 arcsec^2 for ^{12}CO and 600 arcsec^2 for all other species.

[b] All models use $T = 50$ K, $n(H_2) = 5 \times 10^4$ cm^{-2} and $\Delta V = 1$ km s^{-1}. The adopted column densities are listed in Table 7.

Table 6 lists the observed integrated radiation temperatures, corrected for beam efficiency and dilution, grouped by molecule. The upper limits are 2σ values, where σ is the rms noise per channel. The last two columns show the corresponding values of $\int T_{\rm R} dV$ from our model calculations for $T = 50$ K, $n(H_2) = 5 \times 10^4$ cm^{-3}, $x(e) = 10^{-4}$ and $x(e) = 10^{-5}$ and the best fitting column density for each molecule. These column densities are listed in Table 7. It is seen that in general the models reproduce the observed line strengths well. It is not possible on the basis of the present observations to exclude either of the two models. Table 6 lists predicted intensities for a few unobserved transitions of ^{12}CO, ^{13}CO, C^{18}O, and H_2CO that might be used in the future as tests of the models. As will be discussed elsewhere, the excitation of H_2CO may be particularly sensitive to the electron fraction.

Derivation of the column densities of the carbon monoxide molecule presents particular problems. The higher frequency lines of the main isotopomer ^{12}CO are optically thick and thermalized as described above, but the 1–0 line evidently has $\tau \approx 1$. A good fit to all three lines is obtained for a column density N(CO)$\approx 1.3 \times 10^{17}$ cm^{-2}. If the H_2 column density is of order 5×10^{21} cm^{-2} (see below), this would imply that a significant fraction of the carbon is not in molecular form. However, small changes in the beam–dilution correction would change the $2 \rightarrow 1/1 \rightarrow 0$ intensity ratio to which this solution is rather sensitive.

The observed ^{13}CO $1 \rightarrow 0$ and $2 \rightarrow 1$ lines indicate for this isotopomer $N = (3.9 \pm 0.9) \times 10^{15}$ cm^{-2}. For C^{18}O, $N = 5.0 \times 10^{14}$ cm^{-2} is obtained. This yields a ^{12}CO/^{13}CO abundance ratio of 33 ± 10, and ^{12}CO/C^{18}O$\approx 260 \pm 70$, given the estimated total column density of ^{12}CO. These ratios are approximately 2 times lower than the overall [^{12}C]/[^{13}C] $\approx$ 60 and [^{16}O]/[^{18}O] $\approx$ 500 abundance ratios expected in the solar neighborhood (cf. Langer & Penzias 1990). The abundance ratio ^{13}CO/C^{18}O $\approx 7.8 \pm 2$ inferred from optically thin lines is, however, close to the expected solar–neighborhood value of the double isotope ratio, ([^{13}C] [^{16}O]) / ([^{12}C] [^{18}O]) = 500/60 = 8.3. The uncertainty in the ^{12}CO column density is rather large: this column density has been derived for a larger source than is assumed for the ^{13}CO and C^{18}O emissions. We would expect the tabulated column density for ^{12}CO to be an underestimate for the smaller region that characterizes the emissions of the rarer isotopomers.

5.2. *Column density of H_2*

In order to convert the inferred column densities to relative abundances, the H_2 column density for IC 63 is needed. This quantity can be estimated in several ways.

The first method to determine $N(H_2)$ is to use the density $n(H_2) \approx 5 \times 10^4$ cm^{-3} inferred from our excitation calculations. If the size r in the radial direction is assumed to be the same as the observed size on the plane of the sky, 30″, then $r \approx 0.03$ pc $= 9 \times 10^{16}$ cm. The column density can be estimated by multiplying the size with the volume density :

$$N(H_2) \approx n(H_2) r \approx 4.5 \times 10^{21}\ \mathrm{cm}^{-2}. \tag{8}$$

This estimate only holds if the density does not vary throughout the cloud, but this may well be the best way to determine the total column density.

Another method to estimate the amount of molecular gas is in relation to the amount of dust needed to account for the observed infrared emission. In section 4.3 above, we modeled the submillimeter and far–infrared fluxes as thermal emission from dust particles. Based on the adopted opacity law and a typical interstellar gas/extinction ratio $N_{\rm H} \approx 2N({\rm H_2}) = 1.59 \times 10^{21} A_V$ cm^{-2}, the derived dust temperatures and opacities imply $N({\rm H_2}) = (0.6 - 1.4) \times 10^{22}$ cm^{-2} for $\beta = 2$.

We can also use the method of Hildebrand (1983) to estimate the gas column density from the dust optical depth derived in Sect. 4.3. His Eq. (10c) can be rewritten as :

$$N({\rm H+H_2}) = C_\lambda \frac{\tau(\lambda)}{\mu} = C_{\lambda_0} \left(\frac{\lambda}{\lambda_0}\right)^\beta \frac{\tau(\lambda)}{\mu}. \qquad (9)$$

Here μ is the mean mass of the gas particles in grams and C_λ is a coefficient constrained from observations of the reflection nebula NGC 7023. Hildebrand (1983) lists the values $\mu = 1.36 m_{\rm H}$ and $C = 10$ g cm^{-2} at 250 μm. If we substitute $\tau(800) = 2.8 \times 10^{-4}$ and $\beta = 2.0$ we find $N({\rm H_2}) \approx N({\rm H+H_2}) = 1.3 \times 10^{22}$ cm^{-2}. These estimates based upon the thermal dust emission are probably an overestimate because they use a dust temperature compatible with the large–beam flux ratio at 60 and 100 μm and an optical depth normalized to the small–beam submillimeter fluxes. It is possible that the effective dust temperature within the central 20″ × 30″ is higher than the adopted value of $T_{\rm d}$ = 30.5 K. The surface brightnesses at 800 and 450 μm alone would suggest $T_{\rm d}$ = 45 K and $N({\rm H_2}) = 5.5 \times 10^{21}$ cm^{-2}.

Finally, the hydrogen column density can also be inferred from CO by means of the conversion factor $X \equiv \int T_R(1 \rightarrow 0) dV / N({\rm H_2})$. Using $X = 2.5 \times 10^{20}$ K km s^{-1} cm^2 (cf. Bloemen 1989) and assuming that the same factor applies to 2 → 1 emission, we find $N({\rm H_2}) \approx 8 \times 10^{21}$ cm^{-2}. This is quite consistent with the results of the other methods. This agreement is probably fortuitous: the conventional conversion factor applies to optically thick line emission from a virialized cloud radiating at a temperature $T_{\rm ex} \approx 10$ K, yet we have already demonstrated that the temperature in IC 63 is at least 40 K and that the mass is probably far too small for the cloud to be in virial balance at a linewidth $\Delta V \geq 1$ km s^{-1}.

Although the uncertainties in all three methods are rather large, our best estimate of the H$_2$ column density is $N({\rm H_2}) = (5 \pm 2) \times 10^{21}$ cm^{-2}.

5.3. Abundances

We have computed relative abundances $X = N/N({\rm H_2})$ using $N({\rm H_2}) = 5 \times 10^{21}$ cm $^{-2}$. These abundances are listed in Table 7, along with the values found in the "standard" dark clouds TMC–1 and L134 N (Ohishi et al. 1992; Irvine et al. 1987 and references therein). The uncertainties in the IC 63 values are estimated to be about a factor of two. This is primarily a result of the uncertainty in the H$_2$ column density and the electron fraction. The current abundances differ by factors of 2–3 from the values listed by Jansen et al. (1992), mostly because a higher hydrogen density and column density and electron fraction have been adopted in this work.

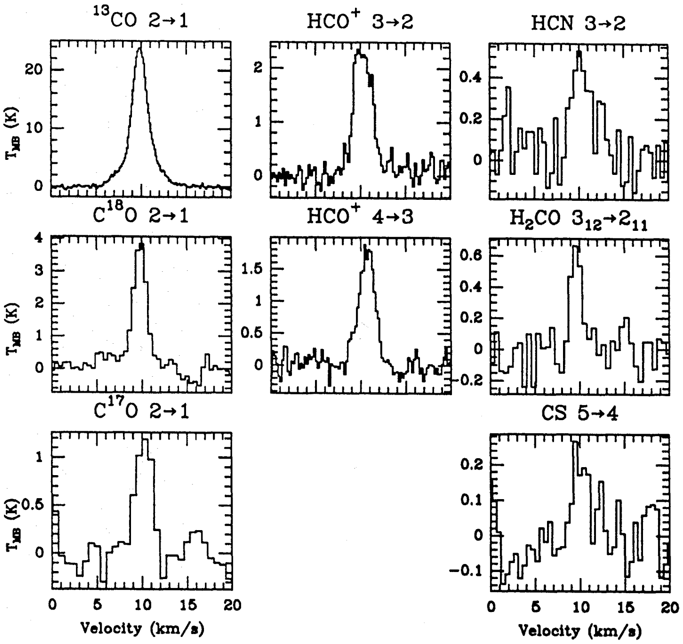

Fig. 7. Examples of spectra of NGC 2023 taken at the various telescopes, converted to $T_{\rm MB}$–scale. The C^{17}O 2→1 and HCO$^+$ 4→3 spectra were taken at the JCMT, the remaining spectra at the CSO

The HCN and HNC column densities are particularly affected by electron collisions. If the electron fraction is as low as 1×10^{-5}, N(HCN) and N(HNC) are increased by a factor $\approx 3 - 4$ compared to the values found for $x(e) = 1 \times 10^{-4}$. The column densities of other species vary by up to 50% for $x(e) = 1 \times 10^{-5}$–1×10^{-4}.

5.4. Effects of gradients

Gradients, both in the physical conditions and in the molecular abundances, can play an important role in a small PDR like IC 63. The small angular extent of the cloud makes it difficult to get any observational evidence for such a gradient. Along the major axis of the cloud we find only a small gradient in radial velocity and very little indication of gradients in any of the other observable properties. Especially the very similar distribution of the CO 2 → 1 and 3 → 2 emission (Fig. 2) indicates that there cannot be much variation in density through the nebula.

To investigate the effects of a possible temperature gradient through the cloud, we constructed a model with 50 % of the molecules in gas of 20 K, and 50 % in gas of 50 K. Because the cloud is small, the temperature is unlikely to fall below 20 K. Examples of the results for a few typical molecules are shown in Table 8. We find at most a 15% decrease in the derived total column density of the molecules. This is because the low excitation lines become stronger at lower temperatures, thus requiring less column density to fit the observed intensity. The effect is smaller than the observational uncertainties in the lines we observed. Only for high excitation lines, such as CO 4 → 3, would the effect of a temperature gradient become significant.

1994A&A...282..605J

Table 7. Column densities and abundances

	IC 63				NGC 2023		TMC-1[a]	L134 N[a]
	$x(e) = 1 \times 10^{-4}$		$x(e) = 1 \times 10^{-5}$					
Species	N(cm^{-2})	X	N(cm^{-2})	X	N(cm^{-2})	X	X	X
H_2	5 (21)	1.0	5 (21)	1.0	5.0 (22)	1.0	1.0	1.0
CO	1.3 (17)	2.6 (-5)	1.3 (17)	2.6 (-5)	5.0 (18)	1.0 (-4)	8 (-5)	8 (-5)
^{13}CO	3.9 (15)	7.8 (-7)	3.9 (15)	7.8 (-7)	5.0 (16)	1.0 (-6)	4 (-6)	4 (-6)
$C^{18}O$	5.0 (14)	1.0 (-7)	5.0 (14)	1.0 (-7)	4.2 (15)	8.4 (-8)	...	1 (-7)[c]
$C^{17}O$	...	...	...	...	2.2 (15)	4.4 (-8)	...	...
CS	6.5 (12)	1.3 (-9)	9.5 (12)	1.9 (-9)	6.9 (13)	1.4 (-9)	1 (-8)	1 (-9)
CN	2.5 (13)	5.0 (-9)	2.7 (13)	5.4 (-9)	<2.0 (13)	<4.0 (-10)	3 (-8)	<3 (-9)
HCN	7.0 (12)	1.4 (-9)	4.0 (13)	8.0 (-9)	5.4 (13)	1.1 (-9)	2 (-8)	4 (-9)
HNC	4.1 (12)	8.2 (-10)	1.1 (13)	2.2 (-9)	<1.2 (12)	<2.4 (-11)	2 (-8)	6 (-9)
HCO^+	6.0 (12)	1.2 (-9)	8.0 (12)	1.6 (-9)	3.0 (13)	6.0 (-10)	8 (-9)	8 (-9)
H_2CO	3.0 (12)	6.0 (-10)	5.0 (12)	1.0 (-9)	3.0 (13)	6.0 (-10)	2 (-8)	2 (-8)
CH_3OH	<1.9 (13)	<3.8 (-9)	...	...	<1.0 (14)	<2.0 (-9)	2 (-9)	3 (-9)
C_2H	2.0 (13)	4.0 (-9)	1.8 (13)	3.6 (-9)	<2.0 (13)	<4.0 (-10)	8 (-8)	<5 (-8)
N_2H^+	2.2 (11)	4.4 (-11)	2.9 (11)	5.8 (-11)	...	...	5 (-10)	5 (-10)
HC_3N	<9.3 (12)	<1.9 (-9)	...	...	...	...	6 (-9)	2 (-10)
HNCO	<2.8 (12)	<5.6 (-10)	...	...	<2.0 (12)	<4.0 (-10)	2 (-10)	...
CH_3CN	<7.4 (12)	<1.5 (-9)	...	...	...	...	1 (-9)	<1 (-9)
H_2S	7.3 (12)	1.5 (-9)	...	...	2.5 (13)	5.0 (-10)	<5 (-10)	8 (-10)
SO	<5.0 (12)	<1.0 (-9)	...	...	<3.0 (14)	<6.0 (-9)	5 (-9)	2 (-8)
SO_2	<1.5 (12)	<3.0 (-10)	...	...	...	...	<1 (-9)	4 (-9)
SiO	<1.0 (12)	<2.0 (-10)	...	...	...	...	<4 (-12)[b]	<2 (-12)[b]

[a] From Ohishi et al. (1992), unless indicated otherwise. [b] Ziurys et al. (1989) [c] Swade (1989)

Table 8. Model with two temperatures[a]

Molecule	Line	W (K km s^{-1})				
		Observed	20 K	50 K	Sum	N_{total} (cm^{-2})
$C^{18}O$	$1 \rightarrow 0$	0.31	0.21	0.08	0.29	4.4 (14)
	$2 \rightarrow 1$	<0.71	0.41	0.32	0.73	...
CS	$2 \rightarrow 1$	1.25	0.63	0.85	1.48	9.0 (12)
	$3 \rightarrow 2$	0.80	0.27	0.48	0.75	...
	$5 \rightarrow 4$	<0.15	0.01	0.06	0.07	...
HCO^+	$1 \rightarrow 0$	7.4	2.61	3.67	6.28	8.0 (12)
	$3 \rightarrow 2$	1.45	0.39	0.97	1.36	...
	$4 \rightarrow 3$	0.45	0.09	0.38	0.47	...

[a] Both temperature components have $n = 5 \times 10^4$ cm^{-3} and $x(e) = 1 \times 10^{-5}$.

More detailed models should include the heating and cooling of both the gas and the dust as functions of depth into the cloud. Such a self-consistent model of the physics and chemistry in this PDR is currently being constructed and will be published in a subsequent paper.

6. NGC 2023 results

In order to investigate whether the results for IC 63 are unique, some molecules have also been observed in the NGC 2023 reflection nebula. The data are summarized in Table 9 and a number of spectra are presented in Fig. 7. The measurements were performed at the position 80″ south of HD 37903, where Black & van Dishoeck (1987) have modeled the H_2 infrared fluorescent emission with $T \approx 80$ K, $n(H_2) \approx (1-5) \times 10^4$ cm^{-3} and an enhancement of the radiation field of about 300. These physical parameters are very similar to those inferred for IC 63.

The analysis of the data proceeded in the same way as for IC 63. Because the NGC 2023 nebula is extended over at least 3′ × 3′ (Gatley et al. 1987; White et al. 1990), no further corrections for beam dilution have been applied since all observations were obtained in beams smaller than 30″. The density has been constrained to $n(H_2) \approx 5 \times 10^4$ cm^{-3} from the observed HCO^+ 3–2/4–3 ratio. The ^{12}CO 2–1 and 3–2 peak main-beam, Rayleigh–Jeans brightness temperatures $T_{\mathrm{MB}} \approx 51$ and 50 K, respectively, correspond to excitation temperatures in excess of 57 K and are consistent with a kinetic temperature $T \approx 80$ K (see also Jaffe et al. 1990). Unfortunately, the temperature-sensitive $3_{03}-2_{02}$ and $3_{22}-2_{21}$ of H_2CO lines were too weak for detection. We adopt $T \approx 80$ K in the analysis.

The resulting column densities for these conditions are listed in Table 7. For species without detailed excitation calculations, the rotation diagram method was again adopted with $T_{\mathrm{rot}} \approx 10$ K. The main uncertainty in deriving the abundances is the appropriate H_2 column density, since the line of sight is perpendicular to the cloud and therefore samples not only the PDR, but also the rest of the dense molecular cloud lying behind it. The $C^{17}O$ 2–1 column density suggests an H_2 column density of 8×10^{22} cm^{-2}, if standard isotope and CO abundances are assumed. This is an order of magnitude larger than found for IC 63. The $C^{18}O$ 3–2

Table 9. Observations and Gaussian fit parameters : NGC 2023

Species	Transition	ν (MHz)	$T_{\rm MB}$ (K)	ΔV (km s^{-1})	$\int T_{\rm MB} dV$ (K km s^{-1})	Telescope	Beam ($''$)	Resolution (MHz)	rms^a (K)
CO	$2 \rightarrow 1$	230538	51.4	3.9	269.	CSO	31	0.5	0.70
	$3 \rightarrow 2$	345796	49.8	5.0	208.	CSO	21	0.5	0.80
^{13}CO	$2 \rightarrow 1$	220399	22.8	2.3	56.4	CSO	33	0.1	0.17
C^{18}O	$2 \rightarrow 1$	219560	4.9	1.8	9.3	CSO	33	0.1	0.15
	$3 \rightarrow 2$	329331	4.8	1.7	8.7	JCMT	15	0.2	0.25
C^{17}O	$2 \rightarrow 1$	224714	1.58	2.0	3.3	JCMT	22	0.2	0.20
CS	$5 \rightarrow 4$	244936	0.31	2.6	0.82	CSO	29	0.5	0.10
CN	$3 \rightarrow 2$	340200	<0.20	...	...	JCMT	15	0.2	0.10
HCN	$3 \rightarrow 2$	265886	0.46	3.0	1.47	CSO	27	0.1	0.10
	$4 \rightarrow 3$	354505	<0.20	...	...	JCMT	14	0.2	0.10
HNC	$1 \rightarrow 0$	90664	<0.15	...	...	IRAM	28	0.1	0.08
HCO$^+$	$3 \rightarrow 2$	267558	2.44	2.4	6.24	CSO	27	0.5	0.11
	$4 \rightarrow 3$	356734	1.77	2.1	3.97	JCMT	14	0.2	0.15
H_2CO	$3_{0,3} \rightarrow 2_{0,2}$	218222	<0.15	...	...	JCMT	23	0.2	0.08
	$3_{1,2} \rightarrow 2_{1,1}$	225698	0.61	1.3	0.83	CSO	32	0.1	0.05
	$3_{1,2} \rightarrow 2_{1,1}$	225698	0.49	1.3	0.70	IRAM	11	0.6	0.12
	$3_{2,2} \rightarrow 2_{2,1}$	218476	<0.15	...	...	JCMT	23	0.2	0.08
	$5_{1,5} \rightarrow 4_{1,4}$	351769	<0.15	...	...	JCMT	14	0.2	0.08
CH_3OH	$5_K \rightarrow 4_K$	241700	<0.14	...	...	CSO	30	0.5	0.07
C_2H	$4 \rightarrow 3$	349400	<0.10	...	...	JCMT	14	0.2	0.05
HNCO	$6_{0,6} \rightarrow 5_{0,5}$	131886	<0.10	...	...	IRAM	19	0.5	0.05
H_2S	$1_{1,0} \rightarrow 1_{0,1}$	168763	1.24	1.1	1.42	IRAM	15	0.1	0.20
SO	$2,2 \rightarrow 1,1$	86094	<0.20	...	...	IRAM	29	0.1	0.10
	$9,8 \rightarrow 8,7$	346528	<0.10	...	...	JCMT	14	0.2	0.05

All observations refer to $\alpha(1950)=05^h39^m07^s.3$, $\delta(1950)=-02^o18'18''.3$. All upper limits are 2σ.

^{a} rms noise per resolution element

data, which should sample only the warmer gas with $T > 30$ K, give a smaller column density of 2.5×10^{22} cm^{-2}, which can be compared with 5.6×10^{22} cm^{-2} deduced from C^{18}O 2–1 (Jaffe et al. 1990). We adopt $N(H_2)\approx$ $(5 \pm 2) \times 10^{22}$ cm^{-2}. This column density is large compared with the column density of warm gas with $T > 100$ K derived from CO 7–6 and ^{13}CO 6–5 observations (Jaffe et al. 1990; Graf et al. 1990), which lies in the range $10^{21} - 10^{22}$ cm^{-2}. Thus, most of the gas appears to have temperatures in the 20–80 K range. As in the case of IC 63, a possible temperature gradient in this range does not significantly affect the results.

The corresponding abundances of the molecules are included in Table 7. In general, they are comparable to, or lower than, those found for IC 63.

7. Comparison between the clouds

Table 7 shows that the derived abundances of simple species such as CS and CN in IC 63 are comparable to those found in TMC–1 and L134 N, especially when the large range of values found for these two clouds is taken into account. However, the abundances of molecules such as HNC, HCO$^+$, H_2CO, N_2H^+, SO and possibly C_2H appear significantly lower by at least a factor of 3 compared with the lowest value found in either of the dark clouds, especially in the model with $x(e) = 1 \times 10^{-4}$. Only the H_2S molecule appears to be more abundant than in the dark clouds : $X = 1.5 \times 10^{-9}$ in IC 63 versus $X = 8 \times 10^{-10}$ in L134 N and $X < 5 \times 10^{-10}$ in TMC–1. Similar statements apply to NGC 2023, even though it has an order–of–magnitude larger total column density.

The underabundances can be naturally explained by the enhanced photodissociation rates in IC 63, where the ultraviolet flux is 650–900 times the mean interstellar radiation field. However, it is not clear why CS, CN and H_2S would be less affected in this case, because there appears to be no deficit of stellar photons at wavelengths below 1200 Å. The high H_2S abundance is especially surprising, since this molecule is rapidly photodissociated by longer–wavelength photons (van Dishoeck 1988). Also, the similar abundances in NGC 2023 are puzzling since this cloud has an order of magnitude larger column density and should thus be less affected by photodissociation. The low abundances of the ions HCO$^+$ and N_2H^+ could result from rapid dissociative recombination with the abundant electrons in this cloud. Theoretical chemical models may help to elucidate these points and will be described in a subsequent paper.

The HCN/HNC abundance ratio is approximately 2-4 in IC 63, which is somewhat higher than the ratio of 1 found in cold clouds. It is significantly lower than the values of 100 or more found in NGC 2023 and in warm regions such as the Orion plateau and IRC +10216 (Irvine et al. 1987; Goldsmith et al. 1986; Schilke et al. 1992). This may provide additional clues about the chemistry in this source. Ion–molecule reactions are expected to produce a constant abundance ratio of order unity, and any deviations from this value might be due to a reaction with a small activation energy (≈ 200 K) which selectively removes HNC. The low ratio in IC 63 indicates that the reaction which causes this ratio to deviate from unity is not very active in IC 63, and that the temperature of the gas containing HCN and HNC is not much higher than 50 K. The higher HCN/HNC ratio in NGC 2023 is consistent with the higher temperature in this source.

The fact that the strong molecular emission is concentrated in a very small part of the cloud suggests that photodissociation may play an even more important role in the outer parts of the nebula. The densest part is partially shielded from the stellar ultraviolet radiation by the dust and the large column density of H_2 and CO. The much lower molecular content of IC 59 could then be explained by a lower total column density of dust and gas. From this simple picture it is expected that the tail of IC 63 should show strong emission from neutral atoms and ions, formed when the molecules are photodissociated and photoionized.

IC 63 contains a molecular cloud of small size and tiny mass. The associated reflection nebula IC 59 appears to be largely devoid of molecules. This raises the question whether IC 63 might be the last surviving dense core of a former, extensive molecular cloud. NGC 2023 is a much larger cloud, whose chemical abundances are similar to those of IC 63 despite its rather larger mean column density. Perhaps NGC 2023 can be described as a system of numerous cores — each like the IC 63 cloud — whose surrounding diffuse molecular envelope has not yet been dissipated and dissociated. Comparative observations of line emission (e.g. H I, [C I], [C II]) from the atomic components of IC 63 and NGC 2023 will be instructive, and such observations are underway.

8. Conclusions

We have observed various molecules in the nearby PDR IC 63. From the observed line intensities we derive $T \approx 50\,\mathrm{K}$ and $n(\mathrm{H_2}) \approx 5 \times 10^4\,\mathrm{cm}^{-3}$. The inferred abundances of some molecules are similar to those found in cold dark clouds, but those of other species are significantly lower. The lower abundances in IC 63 most likely result from the enhanced photodissociation rates. Volatile molecules such as H_2CO, and probably also CH_3OH, CH_3CN and HNCO, and sulfur-oxide molecules such as SO and SO_2, also have low abundances compared to the dark clouds. H_2S, on the other hand, is more abundant in IC 63 by at least a factor of 2. Observations of other nearby nearly–pure PDRs such as NGC 7023 (Fuente et al. 1990, 1993) will be valuable in order to determine whether the conclusions found for IC 63 apply more generally. The limited observations of NGC 2023 clearly point in the same direction. Further work is in progress, including detailed chemical modeling of the IC 63 cloud and self-consistent modeling of the thermal balance.

Acknowledgements. The authors are grateful to the CSO, IRAM and Kitt Peak staff for support during the observations, to T.G. Phillips for assistance during the CSO runs, to F. Baas for performing the JCMT continuum observations, and to M. Hogerheijde for obtaining the NRAO H_2CO observations. They thank the referee, J. Martín-Pintado, for his critical reading of the manuscript and his useful comments. They are indebted to the Netherlands Organization for Scientific Research (NWO) for financial backing. Research in astrochemistry at the University of Arizona is supported by NASA through grant NAGW–2255.

References

Becklin, E.E., Matthews, K., Neugebauer, G., Willner, S.P., 1978, ApJ 220, 831
Black, J.H., van Dishoeck, E.F., 1987, ApJ 322, 412
Black, J.H., van Dishoeck, E.F., 1991, ApJ 369, L9.
Blake, G.A., Sutton, E.C., Masson, C.R., Phillips, T.G., 1987, ApJ 315, 621
Bloemen, J.B.G.M., 1989, ARAA 27, 469
Code, A.D., Meade, M.R., 1979, ApJS 39, 195
Deutsch, L.K., Willner, S.P., 1987, ApJS 63, 803
Dickinson, A.S., Flower, D.R., 1981, MNRAS 196, 297
Dickinson, A.S., Phillips, T.G., Goldsmith, P.F., Percival, I.C., Richards, D., 1977, A&A 54, 645
Draine, B.T., 1978, ApJS 36, 595
Drdla, K., Knapp, G.R., van Dishoeck, E.F. 1989, ApJ 345, 815
Ferlet, R., Vidal-Madjar, A., Laurent, C., York, D.G., 1980, ApJ 242, 576
Fuente, A., Martín–Pintado, J., Cernicharo, J., Bachiller, R., 1990, A&A 237, 471
Fuente, A., Martín–Pintado, J., Cernicharo, J., Bachiller, R., 1993, A&A, in press
Gatley, I., Hasegawa, T., Suzuki, H. et al., 1987, ApJ 318, L73
Goldsmith, P.F., Irvine, W.M., Hjalmarson, Å., Elldér,J., 1986, ApJ 310, 383
Graf, U.U., Genzel, R., Harris, A.I., Hills, R.E., Russell, A.P.G., Stutzki, J., 1990, ApJ 358, L49
Green, S., 1975, ApJ 201, 366
Green, S., 1986, ApJ 309, 331
Green, S., 1991, ApJS 76, 979
Green, S., Chapman, S, 1978, ApJS 37, 168
Green, S., Thaddeus, P., 1974, ApJ 191, 653
Hildebrand, R.H., 1983, QJRAS 24, 267
Irvine, W.M., Goldsmith, P.F., Hjalmarson, Å., (1987) in : Interstellar Processes. D.J. Hollenbach, H.A. Thronson(eds.), Kluwer, Dordrecht, p. 561
Jaffe, D.T., Genzel, R., Harris, A.I., Howe, J.E., Stacey, G.J., Stutzki, J., 1990, ApJ 353, 193
Jansen, D.J., van Dishoeck, E.F., Black, J.H., Phillips, T.G. 1992, in : Astrochemistry of Cosmic Phenomena. IAU Symposium 150. P.D. Singh (ed.), Kluwer, Dordrecht, p. 319
Langer, W.D., Penzias, A.A., 1990, ApJ 357, 477
Mathis, J.S., Mezger, P.G., Panagia, N., 1983, A&A 128, 212
Monteiro, T.S., 1985, MNRAS 214, 419
Monteiro, T.S., Stutzki, J., 1986, MNRAS 221, 33p
Murakami, T., Koyama, K., Inoue, H., Agrawal, P.C., 1986, ApJ 310, L31

Ohishi, M., Irvine, W.M., Kaifu, N., 1992 in : Astrochemistry of Cosmic Phenomena. IAU Symposium 150. P.D. Singh (ed.), Kluwer, Dordrecht, p. 171

Osterbrock, D., 1989, Astrophysics of Gaseous Nebulae and Active Galactic Nuclei. University Science Books, Mill Valley

Schilke, P., Walmsley, C.M., Pineau des Forêts, G., Roueff, E., Flower, D.R., Guilloteau, S., 1992, A&A 256, 595

Schinke, R., Engel, V., Buck, U., Meyer, H., Diercksen, G.H.F., 1985, ApJ 299, 939

Sosin, C., van Dishoeck, E.F., Black, J.H. 1990, unpublished results

Sternberg, A., 1989, ApJ 347, 863

Swade, D.A., 1989, ApJ 345, 828

Troy, B.E., Johnson, C.Y., Young, J.M., Holmes, J.C., 1975, ApJ 195, 643

Turner, B.E., Chan, K–W., Green, S., Lubowicz, D.A., 1992, ApJ 399, 114

Vakili, F., Granes, P., Bonneau, D., Noguchi, M., Hirata, R., 1984, Pub. Astron. Soc. Japan 36, 231

van Dishoeck, E.F., 1988, in: Rate Coefficients in Astrochemistry. T.J. Millar & D.A. Williams, eds., Kluwer, Dordrecht, p. 49.

Wesselius, P.R., Bontekoe, Tj.R., de Jonge, A.R.W., Kester, D.J.M., 1988, in : Astronomy from Large Databases. ESO Conference and Workshop Proceedings, Vol 28. F. Murtagh and A. Heck (eds.)

White, G.J., Sanderson, C., Monteiro, T.S., Richardson, K.J., Hayashi, S.S., 1990, A&A 227, 200

White, N.E., Swank, J.H., Holt, S.S., Parmar, A.N., 1982, ApJ 263, 277

Witt, A.N., Stecher, T.P., Boroson, T.A. Bohlin, R.C., 1989, ApJ 336, L21

Woolf, N.J., Stein, W.A., Strittmatter, P.A., 1970, A&A 9, 252

Ziurys, L.M., Friberg, P., Irvine, W.M., 1989, ApJ 343, 201

This article was processed by the author using Springer-Verlag TEX A&A macro package 1992.